Detection of a cyclotron line in SXP 15.3 during its 2017 outburst

C. Maitra, ¹★ B. Paul, ² F. Haberl, ¹ G. Vasilopoulos ¹
¹Max-Planck-Institut für extraterrestrische Physik, Giessenbachstraße 1, 85748 Garching, Germany

Accepted XXX. Received YYY; in original form ZZZ

ABSTRACT

We report the results of AstroSat and NuSTAR observations of the Be/X-ray binary pulsar SXP 15.3 in the Small Magellanic Cloud during its outburst in late 2017, when the source reached a luminosity level of $\sim 10^{38}~erg~s^{-1}$, close to the Eddington limit. The unprecedented broadband coverage of the source allowed us to perform timing and spectral analysis between 3 and 80 keV. The pulse profile exhibits a significant energy dependence, and morphs from a double peaked profile to a single broad pulse at energies > 15 keV. This can be explained by a spectral hardening during an intensity dip seen between the two peaks of the pulse profile. We detect a Cyclotron Resonance Scattering Feature (CRSF) at ~5 keV in the X-ray spectrum, independent of the choice of the continuum model. This indicates a magnetic field strength of 6×10^{11} G for the neutron star.

Key words: stars: neutron – pulsars: individual: SMC – galaxies: individual: SXP 15.3 – X-rays: binaries

1 INTRODUCTION

SXP 15.3 (aka RX J0052.1-7319) is a transient X-ray binary pulsar located in the Small Magellanic Cloud (SMC), first detected using Einstein observations (Wang & Wu 1992). Later the source was also detected in the ROSAT-PSPC data as a hard and highly variable source and classified as a transient X-ray binary candidate (Kahabka & Pietsch 1996). Coherent pulsations with a period of 15.3 s were discovered in 1996 using ROSAT and CGRO observations with a pulse fraction of 27% at a luminosity (0.1–2 keV) of $\sim 10^{37}$ erg s⁻¹ (Lamb et al. 1999; Finger et al. 2001). Subsequently Kahabka (2000) investigated the ROSAT-HRI observations in 1995 and 1996 and found a large variation in the flux by a factor of ~200, further ascertaining its transient nature. The optical counterpart to the source was identified as a likely Be star by Israel et al. (1999), which was later confirmed as an O9.5IIIe star (V = 14.6 mag, Covino et al. 2001). The source has not been reported in an outburst or a bright state ever since until July 25 2017, when the Swift SMC Survey (S-CUBED) detected a brightening of the source (Kennea et al. 2017). Pulsations at 15.253 s were detected, and the absorption corrected luminosity (0.5-10 keV) corresponded to 2.4×10^{37} erg s⁻¹. The optical counterpart also exhibited a corresponding brightening. The source re-brightened again in November 2017, reaching a higher X-ray luminosity of 3.9×10^{37} erg s⁻¹ (Ducci et al. 2017). This triggered several Target of Opportunity observations (ToO).

In this letter, we present the broadband timing and spectral characteristics of SXP 15.3 for the first time, using AstroSat and NuSTAR observations performed during the recent outburst which

started in October 2017. In Sect. 2 we describe the observations and data reduction. We present the results of a timing analysis (Sect. 3), a spectral analysis (Sect. 4) and pulse phase-resolved spectroscopy (Sect. 5). Discussions and conclusions are presented in Sect. 6.

2 OBSERVATIONS AND DATA REDUCTION

Following the report of an outburst in November 2017, SXP 15.3 was observed with NuSTAR (Harrison et al. 2013) on 2017-11-30 for ~70 ks as a ToO observation. A simultaneous Swift/XRT (Burrows et al. 2005) observation was also carried out for 3 ks (Obsid 00088639001). In addition, we triggered a ToO observation of the source with AstroSat (Agrawal 2006; Singh et al. 2014). The observation was performed on 2017-12-08 with an exposure of 60 ks. The simultaneous Swift and NuSTAR observation will be referred hereafter as Obs. 1 and the AstroSat observation as Obs. 2.

NuSTAR consists of two independent focal plane modules FPMA and FPMB. The data were processed from both the modules using the standard NuSTARDAS software (version 1.8.0 of HEASOFT v.6.22.1 and CALDB version 20171002) to extract barycentercorrected light curves, spectra, response matrices and effective area files. The source events were extracted using a circular region of radius 49" and background events were extracted using a circle of same radius, away from the source.

The Swift/XRT data were analysed following standard procedures described in the Swift data analysis guide¹. The source and background events were extracted using circles of radii 45". The

²Raman Research Institute, C.V. Raman Avenue, Sadashivanagar, Bangalore 560064, India

^{*} E-mail: cmaitra@mpe.mpg.de

http://www.swift.ac.uk/analysis/xrt/

2 C. Maitra et al.

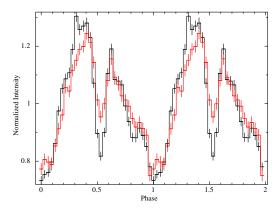


Figure 1. Background subtracted pulse profiles of SXP 15.3, obtained from the FPMA detector of *NuSTAR* (3–79 keV, black) and LAXPC10 of *AstroSat* (3–80 keV, red).

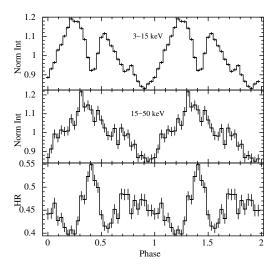


Figure 2. Background subtracted pulse profiles of SXP 15.3 obtained from LAXPC10 of *AstroSat* in the two energy bands of 3–15 keV and 15–50 keV and the HR variation with the pulse phase.

task xrtpipeline was used to generate the *Swift/XRT* spectrum. The response file was generated by using the task XRTMKARF.

AstroSat consists of five independent instruments for performing simultaneous broadband observations. We analysed here data from the Soft X-ray Telescope (SXT) and the Large Area Xenon Proportional Counter (LAXPC). SXT is a focusing telescope consisting of a CCD camera working in the energy range of 0.3–8 keV (Singh et al. 2014). We used level2 data (reprocessed from the level2 pipeline version 1.4a) and merged the event files using sxtevtmergertool. We extracted the spectrum thereafter using XSELECT v2.4². The source events were extracted using an annular region between 1'and 16', and an appropriate on-axis ARF was used for the spectral analysis. Blank sky SXT observations are used to extract the background spectrum.

The LAXPC consists of three co-aligned identical X-ray proportional counters having an absolute time resolution of $10 \,\mu s$ in the energy range 3.0–80.0 keV (Antia et al. 2017; Agrawal et al. 2017). Data were obtained in the Event Analysis mode, level1 products of

which were reprocessed with the LAXPC data analysis software³ to produce light curves and spectral files. The events were filtered for the times corresponding to Earth occultation, passage of the South Atlantic anomaly (SAA) and for large angle offsets of the detectors pointing away from source. The LAXPC background was taken from the same observation in periods when the source was occulted by Earth. LAXPC20 had a different gain during this observation, as determined from the k-fluorescent pulse amplitudes of the double events. A gain factor was used to accommodate the same. All the three LAXPC30 were used for the timing analysis. Due to a gas leakage in LAXPC30 leading to a loss of efficiency, LAXPC30 was excluded from the spectral analysis.

3 TIMING ANALYSIS

We extracted light curves at 100 ms time resolution for the timing analysis. We used the pulse folding and χ^2 -maximisation method to estimate the barycentric corrected pulse period of the pulsar. Pulsations were detected at 15.2563±0.0005 s in Obs. 1 and 15.2575±0.0009 s in Obs. 2 respectively. The errors correspond to 1σ confidence. In the case of the LAXPC detectors (AstroSat), background subtraction was performed by subtracting the background count rates in the energy bands concerned. Fig. 1 shows the background subtracted pulse profiles from AstroSat and NuS-TAR. Pulsations are detected up to 50 keV, and the pulse profiles from both the observations exhibit a double peaked profile which morphs to a single broad pulse at energies > 15 keV (Fig. 2). The pulse fraction was computed as the ratio of $(I_{max} - I_{min})/(I_{max} + I_{min})$. The pulsed fraction increases from 30% in the energy range of 3-5 keV to 60% in the energy range of 30-50 keV in Obs. 1, and from 20% in the energy range of 3-5 keV to 40% in the energy range of 30-50 keV in Obs. 2. The disappearance of the double-peaked nature of the pulse profile with energy motivated us to investigate the hardness ratio (HR) along the spin phase of the system in two energy bands, 3-15 keV and 15-50 keV (Fig. 2). The HR was defined as the ratio of intensity in the 15-50 keV band divided by the 3-15 keV band. The HR shows significant evolution with the spin phase with a spectral hardening seen at the dip phase (phase ~ 0.5).

4 BROADBAND SPECTRAL ANALYSIS

Spectral analysis was performed using XSPEC v12.9.1. We grouped the spectra to achieve a minimum of 20 counts per spectral bin for the analysis. We investigated the broadband spectrum of SXP 15.3 using simultaneous Swift/XRT and NuSTAR data (Obs. 1) and SXT and LAXPC data (Obs. 2). The spectra were modelled with standard continuum models like a power-law with quasi exponential high energy cutoff having various functional forms (XSPEC models 'highecut', 'bknpow', 'fdcut' and 'newhcut'). Other continuum models are a combination of two power laws with different photon indices but a common cutoff energy value called the Negative and Positive power laws with Exponential model (XSPEC model 'NPEX'), and a thermal Comptonization model (XSPEC model 'CompTT'). In order to account for the photoelectric absorption by the interstellar gas, two components were used. The first component was fixed to the Galactic value of 6×10²⁰ cm⁻² (Dickey & Lockman 1990). The second component was left free to account for the absorption within the SMC. For the latter component, the

² http://www.tifr.res.in/~astrosat_sxt/page1_data_ analysis.php

³ http://www.rri.res.in/~rripoc/

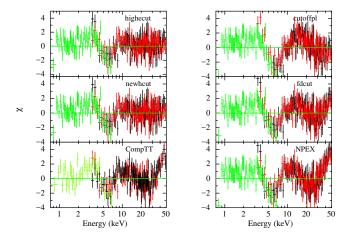


Figure 3. The residuals of the spectral fits with *Swift/XRT* (in green), and FPMA (in black) and FPMB (in red) detectors onboard *NuSTAR* (Obs. 1). The continuum models are mentioned in the panels. An absorption feature at ~5 keV is not included in the fits.

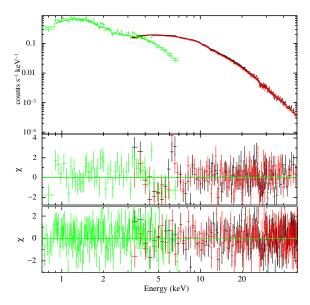


Figure 4. The upper panel shows the best-fit spectral model of SXP 15.3 using spectra from *Swift*/XRT (in green), and FPMA (in black) and FPMB (in red) detectors onboard *NuSTAR* (Obs. 1). The second panel shows the residuals after the fit without taking into account the CRSF and the Fe line. The third panels shows the residuals after including all the model components.

metal abundances were fixed at 0.2 solar, as is typical in the SMC (Russell & Dopita 1992). The atomic cross-sections were adapted from Verner et al. (1996). The X-ray absorption was modelled using the XSPEC model 'tbabs'. Finally, to account for inter-calibration uncertainties of the instruments and small flux variations of the source during not fully simultaneous observing intervals (Obs. 1) we introduce normalisation factors between instruments.

We obtained the best fit to the continuum with the 'newhcut' model. This model is a modified version of 'highecut' which has a smoothed region around the cutoff energy. The smoothing function is a third order polynomial with continuous derivatives (Burderi et al. 2000). An iron fluorescence emission line at \sim 6.4 keV was detected in the *NuSTAR* spectrum. Additionally, a narrow absorption feature was visible at \sim 5 keV in the broadband spectra of Obs.

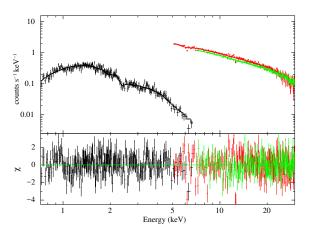


Figure 5. Same as in Fig. 4 using spectra from the SXT (in black), LAXPC10 (in red) and LAXPC20 (in green) onboard *AstroSat* (Obs. 2). The lower panel shows the residuals after including all the model components

1 and Obs. 2, irrespective of the continuum model used (Fig. 3). Addition of a Gaussian absorption feature (*XSPEC* model 'Gabs') improved the fit significantly and the reduced χ^2 after adding the absorption feature decreased to ~1. Table 1 summarises the best-fit broadband spectral parameters and Figs. 4 and 5 show the broadband spectra from Obs. 1 and Obs. 2, respectively. The continuum parameters are consistent between Obs. 1 and Obs. 2. with an indication of spectral softening in Obs. 2. The absorption corrected broadband luminosity (0.5–50 keV) is 9.1×10^{37} ergs s⁻¹ for Obs. 1 and 1.2×10^{38} ergs s⁻¹ for Obs. 2 respectively.

An absorption feature detected in the energy spectrum of HMXB pulsars is reminiscent of a cyclotron resonance scattering feature (CRSF). A careful modelling of the broadband continuum spectrum is essential to detect and model shallow features such as the CRSFs (see for example Müller et al. 2013). Although in this case the addition of the line was required for all the tested continuum models, the line width was narrowest and best constrained with the 'newhout' model (Fig. 3). The improvement in χ^2 after adding the CRSF to the 'newhcut' model was significant, with $\Delta \chi^2 = 75.39$ for 3 d.o.f. in the case of Obs. 1, and $\Delta \chi^2 = 155$ for 3 d.o.f. in the case of Obs. 2, respectively. Although, the CRSF was detected more prominently in Obs. 2, we avoided further interpretations of the CRSF and its parameters with this observation as the line lies at the edge of the energy bands for both the SXT and LAXPC detectors and needs to be treated with caution. However an independent detection of the line at the same energy and with an independent instrument gives us confidence on the obtained results.

5 PHASE-RESOLVED SPECTROSCOPY

The variation of the HR with spin phase (Fig. 2) indicates a dependence of the spectral parameters on the changing viewing angle of the neutron star. Motivated by this we performed pulse phase-resolved spectroscopy using the NuSTAR observation. We created good-time-interval files (gti) using the measured pulse period of NuSTAR to extract phase-resolved spectra into five equally spaced phase bins. As the Swift/XRT data lacked the required statistics for the phase-resolved analysis of SXP 15.3 only NuSTAR data were used for the purpose. The 'newhcut' continuum model was used for the spectral fits. The SMC $N_{\rm H}$, the iron line energy and width, and the CRSF width (σ_c) were frozen to the phase averaged value

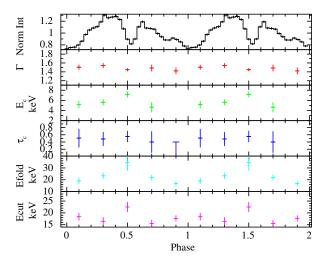


Figure 6. Spectral parameters of SXP 15.3 obtained from the pulse phase-resolved spectroscopy from Obs. 1. The parameters are plotted with 90% confidence. The top panel shows the pulse profile obtained from the FPMA detector (3–79 keV).

in each phase bin. Fig. 6 shows the variation of the spectral parameters with pulse phase. The spectrum is harder at the dip phase as compared to the peaks, i.e. $\Gamma = 1.54 \pm 0.05$ at phase ~ 0.3 to $\Gamma = 1.40 \pm 0.03$ at phase ~0.5. This is consistent with the results obtained from the investigation of the variation of the HR with the pulse phase. The CRSF centroid energy E_c is variable with pulse phase with E_c rising to ~8 keV at the dip phase. E_c varies by a factor of 1.5 ± 0.3 between the dip and the adjacent phase bin (phase ~0.7). The CRSF is not detected at the off-pulse phase which might be due to insufficient statistics in that phase bin. In order to obtain an upper limit on the CRSF depth at this phase, we froze the CRSF energy and width to the phase averaged value and obtained $\tau_c \sim 0.4$. The variation of CRSF parameters with phase is typically seen in many HMXB pulsars, with the pattern of the variations revealing important information on the beaming geometry and the magnetic field geometry of the HMXB pulsar (see Maitra 2017, for a comprehensive summary of phase-resolved analysis of CRSFs).

6 DISCUSSION AND CONCLUSIONS

In this letter we report the broadband X-ray timing and spectral properties of SXP 15.3 for the first time, and at the brightest state of the source detected till today. We also report the discovery of a CRSF at \sim 5 keV. This makes it only the second Magellanic pulsar after SMC X-2 (Jaisawal & Naik 2016) with a cyclotron line detection, and hence a confirmed magnetic field strength of the neutron star. The spin period measurements with the *NuSTAR* and *AstroSat* observations are consistent within errors precluding the detection of any spin-up during the current outburst. The net spin-up rate between the *CGRO* and *ROSAT* observations separated by 123 days was -1.64×10^{-9} s s⁻¹ (Finger et al. 2001). The long term trend in the spin evolution as inferred from the spin period measurements between the *CGRO* and *AstroSat* observations however indicate a much reduced spin-up rate of -2.92×10^{-11} s s⁻¹.

The magnetic field strength of the neutron star can be determined from the observed CRSF centroid energy $E_{\rm cyc}$ (determined

from Obs. 1), and is given as:

$$E_{\rm cyc} = \frac{11.57 \,\text{keV}}{1 + 7} \times B_{12} \tag{1}$$

where B_{12} is the field strength in units of 10^{12} G; $z \sim 0.3$ is the gravitational red shift in the scattering region for standard neutron star parameters. This implies a magnetic field strength of the neutron star of $B = 6 \times 10^{11}$ G, assuming the line forming region lies close to the neutron star surface. The obtained field strength is consistent with the estimate obtained by Christodoulou et al. (2017) assuming that SXP 15.3 was in the propeller state at its lowest detected X-ray luminosity ($L_x \sim 6.8 \times 10^{33}$ erg s⁻¹ as detected from a *Chandra* observation).

The unabsorbed bolometric X-ray luminosity of SXP 15.3 during the observations indicate that the source was accreting near its Eddington limit of 2×10^{38} erg s⁻¹ for a typical neutron star mass of 1.4 M_{\odot} . In highly magnetised accretion powered pulsars, the location and geometry of the radiation emitting region are believed to be dependent on the mass accretion rate (Basko & Sunyaev 1976). At a luminosity of $\sim 10^{38}$ erg s⁻¹ SXP 15.3 is expected to be in the super-critically accreting or radiation-dominated regime. In the super-critical regime, a radiation-dominated shock is formed, after which the accreted matter settles to the neutron star surface in a magnetically confined accretion column. The radiation in this case predominantly escapes from the optically thin sides of the accretion column in a fan-beam like pattern. The critical-luminosity (L_c) , which divides the two regimes of sub and super-critical accretion is a function of the surface magnetic field strength of the neutron star and can be approximated as (Becker et al. 2012):

$$L_{\rm c} = 1.49 \times 10^{37} \rm erg \, s^{-1} \left(\frac{\Lambda}{0.1}\right)^{-7/5} w^{-28/15} \times \left(\frac{M}{1.4 \, \rm M_{\odot}}\right)^{29/30} \left(\frac{R}{10 \, \rm km}\right)^{1/10} \left(\frac{B_{\rm surf}}{10^{12} \, \rm G}\right)^{16/15}$$
(2)

M, R, and B_{surf} are, the mass, radius, and surface magnetic field strength of the neutron star, w = 1 characterises the shape of the photon spectrum inside the column, and Λ is the mode of accretion. $\Lambda = 0.1$ approximates the case of disk accretion, and $\Lambda = 1.0$ is more appropriate for wind accretors. Assuming $\Lambda = 0.1$ and $B_{\rm surf} = 6 \times 10^{11}$ G, results in $L_{\rm c} = 9 \times 10^{36}$ erg s⁻¹ for typical neutron star mass and radius values⁴. This ascertains that SXP 15.3 is accreting in the super-critical regime. The double-peaked pulse profile of SXP 15.3 observed in this work is in further support of the predominance of a fan-beam like emission. The disappearance of the double peak to a single broad peak at higher energies is most likely due to the intrinsic nature of the emission rather than being caused by a local absorbing matter phase locked to the neutron star. This is because we found no evidence of an additional absorption component in the spectral fit of SXP 15.3. A further indication of the fan-beam emission is obtained from the shape of the CRSF. A deep and narrow CRSF, as seen in SXP 15.3 is expected for viewing angles perpendicular to the magnetic field axis, a.k.a. fan-beam like emissions (Schwarm et al. 2017).

The luminosity of SXP 15.3 during Obs. 2 was \sim 30% higher than in Obs. 1, with an indication of spectral softening with increasing luminosity. This behaviour is expected in the super-critical

⁴ A more detailed treatment of critical-luminosity can be found in Mushtukov et al. (2015). We however verified that our obtained L_c is consistent between the two works for the estimated B_{12} value.

Table 1. Best-fitting parameters (with 90% errors) obtained from the spectral fitting with the newhout continuum model with an iron emission line and cyclotron absorption line.

Parameter	Obs. 1		Obs. 2	
	NEWHCUT	NEWHCUT×GABS	NEWHCUT	NEWHCUT×GABS
SMC N _H ^a	0.40±0.09	0.6±0.1	0.31±0.06	0.45±0.06
Photon index	1.40 ± 0.01	$1.48^{+0.06}_{-0.03}$	1.40 ± 0.02	1.40 ± 0.02
E _{cut} (keV)	16.4 ± 0.6	16.9±0.8	18.8 ± 2.0	20.9 ± 2.3
E _{fold} (keV)	26.8 ± 1.4	$28.5^{+2.2}_{-1.7}$	$37.1^{+12.8}_{-10.4}$	$33.4^{+17.6}_{-12.8}$
Fe line energy (keV)	6.39 ± 0.08	6.37 ± 0.08	-10.4	-12.6
Fe line eq. width (eV)	89.7±18	91.4±18	-	-
Cycl. line energy (E _c) (keV)	_	$5.7^{+0.3}_{-0.6}$ $1.7^{+0.8}_{-0.5}$	_	5.2±0.2
Cycl. line width (σ_c) (keV)	_	$1.7^{+0.8}_{-0.5}$	_	0.67 ± 0.17
Cycl. line strength (τ_c)	-	$0.4^{+0.5}_{-0.2}$	-	0.6 ± 0.1
Luminosity ^b	_	0.91±0.05	_	1.2±0.1
Reduced- χ^2 (d.o.f)	1.19 (450)	1.04 (447)	1.39 (582)	1.13 (579)

 $[^]a$: Equivalent hydrogen column density (in 10^{22} atoms cm $^{-2}$); b : Absorption corrected luminosity (0.5–50 keV) in 10^{38} ergs s $^{-1}$, assuming a distance of 61 kpc.

regime, and can be understood either due to a decrease in the plasma temperature with rising accretion column (Becker et al. 2012), or alternatively a lower fraction of the radiation reflected by the neutron star surface in the case of a taller accretion column at higher intensities (Postnov et al. 2015).

The CRSF parameters show little variations with pulse phase. This may indicate no gradient of the properties of the line forming region across the viewing angles. Alternatively, this might also be due to the effect of gravitational light bending near the neutron star surface (Beloborodov 2002) which would smear out the pulse-phase dependence, with a particular viewing angle having contributions from multiple emission regions. The only variable CRSF parameter is the centroid energy E_c which is significantly higher at the dip phase. This suggests that the line forming region at this phase may offer a deep and a more direct view into the emission region along the magnetic axis which is consistent with fan-beam like emission. An indication of spectral hardening at the dip phase is further consistent with a direct view into the emission region along the magnetic axis (see for e.g. Pravdo et al. 1978).

In summary we present the broadband timing and spectral results of SXP 15.3 for the first time using *AstroSat* and *NuSTAR* ToO observations performed during the recent outburst in October 2017. We also report the discovery of a CRSF at \sim 5 keV, establishing the magnetic field of the neutron star at 6×10^{11} G. The CRSF centroid energy varies with pulse phase, with an increase in energy during an intensity dip. This is accompanied with a spectral hardening during the dip. The two signatures mentioned above and the double-peaked pulse profile of SXP 15.3 indicate a fan-beam like geometry dominating the emitting region as is expected for supercritically accreting sources.

ACKNOWLEDGEMENTS

We thank the reviewer for providing useful comments. The authors would like to thank the AstroSat operations team members for scheduling the ToO observation. The authors would also like to thank all the *NuSTAR* and *Swift* team members for ToO observations. CM acknowledges Gulab Dewangan for useful discussions and suggestions on the analysis of the SXT data.

REFERENCES

Agrawal P. C., 2006, Advances in Space Research, 38, 2989

Agrawal P. C., et al., 2017, Journal of Astrophysics and Astronomy, 38, 30 Antia H. M., et al., 2017, ApJS, 231, 10

Basko M. M., Sunyaev R. A., 1976, MNRAS, 175, 395

Becker P. A., et al., 2012, A&A, 544, A123

Beloborodov A. M., 2002, ApJ, 566, L85

Burderi L., Di Salvo T., Robba N. R., La Barbera A., Guainazzi M., 2000, ApJ, 530, 429

Burrows D. N., et al., 2005, Space Sci. Rev., 120, 165

Christodoulou D. M., Laycock S. G. T., Yang J., Fingerman S., 2017, Research in Astronomy and Astrophysics, 17, 059

Covino S., Negueruela I., Campana S., Israel G. L., Polcaro V. F., Stella L., Verrecchia F., 2001, A&A, 374, 1009

Dickey J. M., Lockman F. J., 1990, ARA&A, 28, 215

Ducci L., et al., 2017, The Astronomer's Telegram, 11030

Finger M. H., Macomb D. J., Lamb R. C., Prince T. A., Coe M. J., Haigh N. J., 2001, ApJ, 560, 378

Harrison F. A., et al., 2013, ApJ, 770, 103

Israel G. L., Stella L., Covino S., Campana S., Mereghetti S., 1999, IAU Circ., 7101

Jaisawal G. K., Naik S., 2016, MNRAS, 461, L97

Kahabka P., 2000, A&A, 354, 999

Kahabka P., Pietsch W., 1996, A&A, 312, 919

Kennea J. A., Evans P. A., Coe M. J., Udalski A., 2017, The Astronomer's Telegram, 10600

Lamb R. C., Prince T. A., Macomb D. J., Finger M. H., 1999, IAU Circ., 7081

Maitra C., 2017, Journal of Astrophysics and Astronomy, 38, 50

Müller S., et al., 2013, A&A, 551, A6

Mushtukov A. A., Suleimanov V. F., Tsygankov S. S., Poutanen J., 2015, MNRAS, 447, 1847

Postnov K. A., Gornostaev M. I., Klochkov D., Laplace E., Lukin V. V., Shakura N. I., 2015, MNRAS, 452, 1601

Pravdo S. H., Bussard R. W., Becker R. H., Boldt E. A., Holt S. S., Serlemitsos P. J., 1978, ApJ, 225, 988

Russell S. C., Dopita M. A., 1992, ApJ, 384, 508

Schwarm F.-W., et al., 2017, A&A, 601, A99

Singh K. P., et al., 2014, in Space Telescopes and Instrumentation 2014: Ultraviolet to Gamma Ray. p. 91441S, doi:10.1117/12.2062667

Verner D. A., Ferland G. J., Korista K. T., Yakovlev D. G., 1996, ApJ, 465, 487

Wang Q., Wu X., 1992, ApJS, 78, 391